Connecting Microstructures for Multiscale Topology Optimization with Connectivity Index Constraints

Zongliang Du

Structural Engineering Department,

University of California San Diego, San Diego, CA 92093, USA

zodu@eng.ucsd.edu

Xiao-Yi Zhou

School of Engineering,

Cardiff University, Cardiff, CF24 3AA, UK

zhoux19@cf.ac.uk

Renato Picelli

School of Engineering,

Cardiff University, Cardiff, CF24 3AA, UK

picellir@cf.ac.uk

H. Alicia Kim

Structural Engineering Department,

University of California, San Diego, San Diego, CA 92093, USA

School of Engineering,

Cardiff University, Cardiff, CF24 3AA, United Kingdom

alicia@ucsd.edu

With the rapid developments of advanced manufacturing and its ability to manufacture microscale features, architected materials are receiving ever increasing attention in many physics fields. Such a design problem can be treated in topology optimization as architected material with repeated unit cells using the homogenization theory with the periodic boundary condition. When multiple architected materials with spatial variations in a structure are considered, a challenge arises in topological solutions which may not be connected between adjacent material architecture. This paper introduces a new measure, Connectivity Index (CI) to quantify the topological connectivity and adds it as a constraint in multiscale topology optimization to achieve connected architected materials. Numerical investigations reveal that the additional constraints lead to microstructural topologies which are well connected and do not substantially compromise their optimalities.

1 Introduction

Materials/structures with well-designed microstructures showing excellent properties are ubiquitous in nature, e.g., both high stiffness and toughness of the nacre [1], remarkable bending stiffness of bamboo [2], fascinating colors of the butterfly wings [3]. Furthermore, an increasing attention is seen in design of the metamaterials possessing extraordinary properties that are not commonly found in nature [4-5]. By taking an advantage of the modern manufacturing technology, complex designs of microstructures can be fabricated conveniently [6-8].

Inspired by the inverse homogenization approach [9], many works devoted to design microstructures to tailor properties of architected materials [6-10]. Taking this to the next step, multiscale topology optimization has been developed to simultaneously design a macroscopic structure and the associated material microstructure(s). Rodrigues et al. [11] obtained a hierarchical design by optimizing the periodic microstructures in every macroscale finite element. This method, however, would lead to a very high computational cost particularly for three dimensional cases [12]. As a more computational tractable strategy, Liu et al. [13] proposed the Porous Anisotropic Material with Penalization (PAMP) model to obtain a multiscale structure with a uniform microstructure. This approach has been extended to consider dynamic and thermomechanical effects [14, 15]. Sivapuram et al. [16] recently proposed a more generalized simultaneous structure and material optimization formulation where any number of microstructures can be obtained. They proposed a linearization formulation to decompose the macroscale and microscale optimizations, thereby parallel and distributed computing can be adopted easily.

In majority of the multiscale optimization studies, the asymptotic homogenization theory has been used to obtain the effective material property of a periodic microstructure. The assumption of the scale separation and the periodicity in the homogenization theory [17] ignores the connectivity of the adjacent microstructures [11, 12, 16]. It should be noted that, besides poor manufacturability, more importantly,

poor microstructural connectivity would lead to load transition issue as well as the deviation of effective property estimated by homogenization method. In order to obtain the optimal sizes of microstructures, consider boundary effect as well as guarantee the connectivity between different microstructures, Alexandersen and Lazarov [18] abandoned the homogenization theory and directly optimized the micro-structures with an extremely fine mesh. Even though the authors tried to reduce the computational resource requirements, the computation cost is substantially higher than the homogenization-based approaches. It has been shown that the optimal solution of a unit cell converges rapidly to that obtained by inverse homogenization as the number of repetitive cells increases (beyond five or six in the case of mechanical properties) [19, 20]. In addition, for boundary effect, as shown in [21], the thickness of boundary layer has the same scale of the unit cell. Results in [19-21] suggested that the homogenization method can efficiently offer a reasonable approximation for a large number of repeated unit cells, when some global measures, e.g., mean compliance, are taken into consideration. Liu et al. [22] divided the structural domain into several subdomains and boundary layers. The optimum subdomain periodic microstructures were obtained by inverse homogenization and direct optimization was applied to the boundary layers with an extremely fine mesh to obtain the smooth transitions between different microstructures.

For microstructures with graded properties, the connectivity has been enforced implicitly via fixing some connective elements or applying a pseudo load or adding nonlinear diffusion term to the objective function, [23-25]. Whilst such implicit controls have been shown to be effective in many cases, they cannot guarantee the connectivity (Fig. 1(a)). It may also have an effect of over-constraining the design space.

Another approach for connecting microstructures is to apply a post-processing based on the metamorphosis technique. Wang et al. [26] generated a series of self-similar and connected microstructures by interpolating between a prototype cell and a solid cell. Such an interpolation technique is a well-established practice for the level set method in the field of image processing. However, it can create discontinuous member sizes such as shown in Fig. 1(b) which can lead to stress concentrations. Furthermore,

such an interpolation method may lead to a floating topology that is no longer physical when applied to two cells with distinct topologies, e.g. Fig. 1(c).

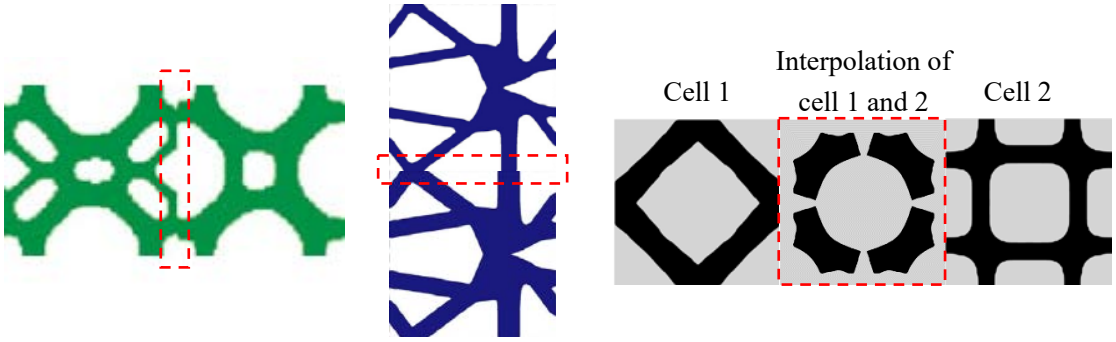

Fig. 1 Challenges seen in the existing methods for connectivity of microstructures: *(a)* imperfect connection by implicit control method [24], *(b)* interface mismatch by shape metamorphosis [26] and *(c)* floating microstructure by shape metamorphosis method

This paper presents a new formulation of multiscale topology optimization with connected microstructures. An explicit Connectivity Index (CI) is introduced as a measure for the connectivity between two adjacent topologies and this quantity is added to the multiscale topology optimization problem. The multiscale optimization formulation introduced by Sivapuram et al. [16] is employed for numerical demonstrations and the level set topology optimization method of Dunning and Kim [27] is used for topology optimization at both macro and microscale.

The remainder of the paper is organized as follows. In Sections 2 and 3, the level set topology optimization method and the multiscale optimization formulations are outlined for completeness. To connect microstructures in multiscale design problems illustrated in Section 3, an explicit CI is proposed in Section 4 and applied to control the microstructural connectivity in Section 5. The CI-constrained optimization approach is applied to obtain optimal multiscale designs with well-connected microstructures in Section 6, followed by some concluding remarks.

2 Level Set Topology Optimization Method

The level set topology optimization method used in this paper follows Dunning and Kim [27] and is briefly summarized in this section.

In the level set method, a structure is implicitly represented by a level function $\phi(\boldsymbol{x})$, (1) and the Hamilton-Jacobi equation expressed by (2) advances the structural interface or boundary,

$$\begin{cases} \phi(\boldsymbol{x}) > 0, & \text{for } \boldsymbol{x} \in \Omega \\ \phi(\boldsymbol{x}) = 0, & \text{for } \boldsymbol{x} \in \Gamma \cap \mathrm{D} \\ \phi(\boldsymbol{x}) < 0, & \text{for } \boldsymbol{x} \in \mathrm{D} \backslash \overline{\Omega} \end{cases} \tag{1}$$

where D is the design domain, Ω is the structural domain, Γ is the structural boundary and $\overline{\Omega}$ is the closure of Ω.

$$\frac{\partial \phi}{\partial t}(\boldsymbol{x}, t) + V_n |\nabla \phi|(\boldsymbol{x}, t) = 0, \qquad \text{for } \boldsymbol{x} \in \Gamma \cap \mathrm{D} \tag{2}$$

with V_n denoting the normal inward velocity of structural boundary and t a pseudo time. The forward Euler scheme is typically used to solve (2) numerically,

$$\phi_i^{k+1} = \phi_i^k - \Delta t \left|\nabla \phi_i^k\right| V_{n,i} = \phi_i^k - \left|\nabla \phi_i^k\right| Z_{n,i} \tag{3}$$

where k is the iteration number, Δt is the time step, $V_{n,i}$ is the normal velocity of the boundary point i and $Z_{n,i}$ is the distance of the associated normal movement.

A general topology optimization problem can be written as

$$\begin{aligned} &\min_{\Omega(\phi)} \ f(\Omega) \\ &\text{s.t.} \quad g_j(\Omega) \leq 0, j = 1, \ldots, m \end{aligned} \tag{4}$$

where f is the objective functional and g_j denotes a constraint functional. With the help of shape derivative, linearizing (4) gives,

$$\begin{cases} \Delta f\left(\Delta\Omega(\boldsymbol{Z}_n)\right) = \int_\Gamma s_f Z_n d\Gamma + o(Z_n) \approx \sum s_f Z_n L = \boldsymbol{C}_f \cdot \boldsymbol{Z}_n \\ \Delta g_i\left(\Delta\Omega(\boldsymbol{Z}_n)\right) = \int_\Gamma s_{g,j} Z_n d\Gamma + o(Z_n) \approx \sum s_{g,j} Z_n L = \boldsymbol{C}_{g,j} \cdot \boldsymbol{Z}_n \end{cases} \tag{5}$$

where s_f and $s_{g,j}$ are the shape sensitivities of the objective and j-th constraint functionals, respectively, and L is the length of a discretized boundary segment. $\boldsymbol{C}_f$ and $\boldsymbol{C}_{g,j}$ are the scaled sensitivity vectors of the objective function and j-th constraint

functionals. $\boldsymbol{Z}_n$ is the vector of boundary movement distance. With further manipulations [16, 27], the optimization problem of (4) at the *k*-th iteration can be transformed to,

$$\begin{aligned} &\min_{\alpha,\boldsymbol{\lambda}} \boldsymbol{C}_f^k \cdot \boldsymbol{Z}_n^k(\alpha,\boldsymbol{\lambda}) \\ &\text{s.t.} \quad \boldsymbol{C}_{g,j}^k \cdot \boldsymbol{Z}_n^k \le -\bar{g}_j^k, j = 1,\dots,m \\ &\boldsymbol{Z}_{n,\min}^k \le \boldsymbol{Z}_n^k \le \boldsymbol{Z}_{n,\max}^k \end{aligned} \tag{6}$$

where $\boldsymbol{Z}_n^k(\alpha,\boldsymbol{\lambda}) = \alpha\left(\boldsymbol{C}_f^k + \sum_{j=1}^m \lambda_j \boldsymbol{C}_{g,j}^k\right)$. The upper and lower bounds, $\boldsymbol{Z}_{n,\min}^k$ and $\boldsymbol{Z}_{n,\max}^k$ are determined by the CFL condition or the limits of the design domain. $\bar{g}_j^k$ is the residual of the j-th constraint at k-th step. The optimization problem of (6) is solved using the open source optimizer NLopt [28] and the solution gives the boundary movement distance $\boldsymbol{Z}_n^k$. This is then substituted into (3) to optimize structural boundaries.

3 Multiscale Optimization

In the multiscale topology optimization framework [16], the design domain D is first divided to a certain number of subregions (i.e., $\mathrm{D}_1,\dots,\mathrm{D}_N$ with $\bigcup_{e=1}^N \mathrm{D}_e = \mathrm{D}$ and $\forall\, \mathrm{D}_e \bigcap \mathrm{D}_l = \emptyset,\ e \ne l; e,l = 1,\dots,N$). An illustrative example is shown in Fig. 2. It is also assumed that uniform microstructures are distributed in each subregion and can be analyzed by the asymptotic homogenization theory. By simultaneously optimizing the macroscopic structure and microscopic unit cells, the design space is greatly extended to improve the functional performance.

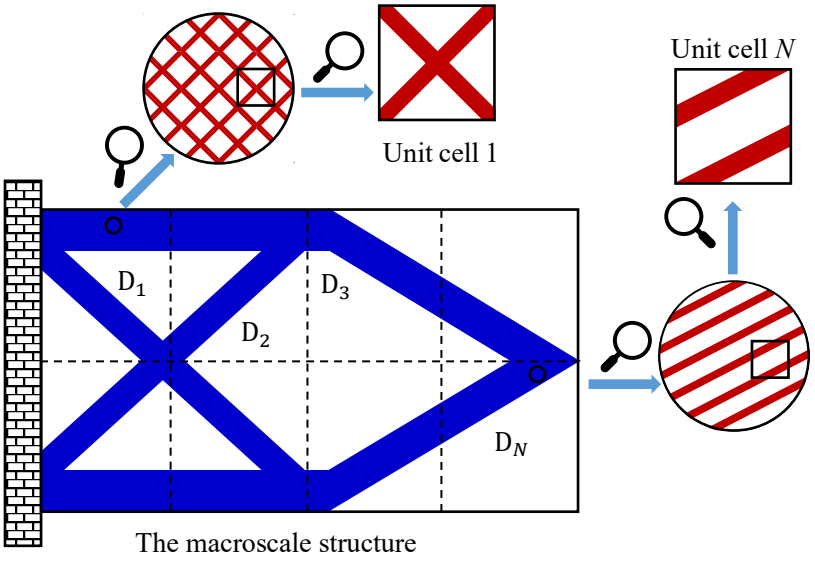

Fig. 2 An illustration of multiscale topology optimization without connectivity

3.1 Formulation

For the case of the compliance minimization, the multiscale topology optimization problem is formulated as follows

$$\text{find } \phi_M(\boldsymbol{x}) \in L^\infty(\mathrm{D}), \phi_{me}(\boldsymbol{y}) \in L^\infty(\mathrm{Y}), \boldsymbol{u}(\boldsymbol{x}) \in \mathbf{H}^1(\mathrm{D}), \boldsymbol{\chi}_e^{pq}(\boldsymbol{y}) \in U_\mathrm{Y}$$

$$(e = 1, \dots, N, p, q = 1,2,3)$$

$$\min \int_\mathrm{D} H(\phi_M) f_i u_i d\Omega + \int_{\Gamma_\mathrm{t}} \bar{t}_i u_i d\Gamma$$

s. t.

$$\int_\mathrm{Y} H(\phi_{me}) \mathbb{E}_{ijpq} \frac{\partial \chi_{e,p}^{kl}}{\partial y_q} \frac{\partial v_i}{\partial y_j} d\mathrm{Y} = \int_\mathrm{Y} H(\phi_{me}) \mathbb{E}_{ijkl} \frac{\partial v_i}{\partial y_j} d\mathrm{Y}, \forall \boldsymbol{v} \in U_\mathrm{Y} \tag{7}$$

$$\mathbb{E}_{e,ijkl}^\mathrm{H} = \frac{1}{|\mathrm{Y}|} \int_\mathrm{Y} \left(\mathbb{E}_{ijkl} - \mathbb{E}_{ijpq} \frac{\partial \chi_{e,p}^{kl}}{\partial y_q} \right) d\mathrm{Y}$$

$$\int_{\cup_{e=1}^{N} \mathrm{D}_e} H(\phi_M)\mathbb{E}^{\mathrm{H}}_{e,ijkl}\frac{\partial u_i}{\partial x_j}\frac{\partial v_k}{\partial x_l}d\Omega = \int_{\mathrm{D}} H(\phi_M) f_i v_i d\Omega + \int_{\Gamma_{\mathrm{t}}} \bar{t}_i v_i d\Gamma, \forall\, \boldsymbol{v} \in U^0_{\mathrm{ad}}$$

$$\int_{\mathrm{D}} H(\phi_M)d\Omega - w_M|\mathrm{D}| \le 0$$

$$\int_{\mathrm{Y}} H(\phi_{me})d\mathrm{Y} - w_{me}|\mathrm{Y}| \le 0$$

where ϕ_M is the macroscopic level set function defined on domain D; ϕ_{me} is the e-th microscopic level set function on domain Y; $\boldsymbol{f}$ is the body force density; $\bar{\boldsymbol{t}}$ is the surface traction applied on the Neumann boundary Γ_{t}; $\boldsymbol{u}$ is the displacement field with the prescribed value $\boldsymbol{u} = \bar{\boldsymbol{u}}$ on the Dirichlet boundary Γ_{u}; $\mathbb{E}$ denotes the elasticity tensor of the base material; $\mathbb{E}^{\mathrm{H}}_{e,ijkl}$ denote the components of the homogenized elasticity tensor in the subdomain D_e; $\boldsymbol{\chi}^{kl}_e$ are the characteristic displacement fields in e-th unit cell; $U_{\mathrm{Y}} = \{\boldsymbol{v}(\boldsymbol{y}), \boldsymbol{y} \in \mathrm{Y} | \boldsymbol{v}(\boldsymbol{y}) \text{ is } \mathrm{Y}-\text{periodic}; \boldsymbol{v} \text{ is smooth enough}\}$ is the space of the Y-periodic solutions of the characteristic displacement field; while $U^0_{\mathrm{ad}} = \{\boldsymbol{v}(\boldsymbol{x}), \boldsymbol{y} \in \mathrm{D} | \boldsymbol{v}(\boldsymbol{x}) \in \mathbf{H}^1(\mathrm{D}), \boldsymbol{v} = \mathbf{0} \text{ on } \Gamma_{\mathrm{u}}\}$ denotes the space of virtual displacement field of the homogenized structure. Instead of using an integrated volume constraint, w_M and w_{me} are the volume fraction upper bounds of the macrostructure and e-th unit cell.

For the multiscale topology optimization problems, Sivapuram et al. [16] suggested to linearize first both the objective function and constraints with the use of their sensitivities with respect to the macro level set function and N micro level set functions. Then the linearized program is decoupled into $N+1$ parallel optimization problems which are involved with either the macro level set function or a single micro level set function. For constraints coupled with both macro and micro level set functions, an inner level program needs to be solved to determine the optimal constraint bounds for the $N+1$ problems. In this problem formulation Eq. (7), since the volume constraints are separately applied on the macroscopic level set function and each microscale level set function, the original formulation can be solved in parallel at each

iteration step. To be specific, in k-th iteration, the macroscale level set function is updated by solving the following sub-level optimization problem:

$$\begin{aligned} &\min_{\alpha,\boldsymbol{\lambda}} \boldsymbol{C}_{f,M}^{k} \cdot \boldsymbol{Z}_{n}^{k}(\alpha,\boldsymbol{\lambda}) \\ &\text{s.t.} \quad \boldsymbol{C}_{M}^{k} \cdot \boldsymbol{Z}_{n}^{k} \le -\bar{g}_{M}^{k}, \\ &\quad \boldsymbol{Z}_{n,\min}^{k} \le \boldsymbol{Z}_{n}^{k} \le \boldsymbol{Z}_{n,\max}^{k} \end{aligned} \tag{8}$$

where $\boldsymbol{C}_{f,M}^{k}$ and $\boldsymbol{C}_{M}^{k}$ are the sensitivity vectors of the macro level set function associated with the objective function and volume constraint, $\boldsymbol{Z}_{n}^{k} = \alpha\left(\boldsymbol{C}_{f,M}^{k} + \lambda \boldsymbol{C}_{M}^{k}\right)$, $\bar{g}_{M}^{k}$ is the residual of macroscale volume constraint and the related shape sensitivities are

$$\begin{cases} \boldsymbol{C}_{f,M}^{k}(\boldsymbol{x}^{B}) = -\left(L\mathbb{E}_{ijkl}^{\mathrm{H}} \varepsilon_{ij}^{k} \varepsilon_{kl}^{k}\right)(\boldsymbol{x}^{B}) \\ \boldsymbol{C}_{M}^{k}(\boldsymbol{x}^{B}) = L(\boldsymbol{x}^{B}) \end{cases} \tag{9}$$

with $\boldsymbol{\varepsilon}^{k}(\boldsymbol{x}^{B})$ denoting the strain tensor and $L(\boldsymbol{x}^{B})$ denoting the corresponding weighted length of boundary point $\boldsymbol{x}^{B}$.

The optimal boundary movement of the level set function of the e-th unit cell is determined by the following program:

$$\begin{aligned} &\min_{\alpha,\boldsymbol{\lambda}} \boldsymbol{C}_{f,me}^{k} \cdot \boldsymbol{Z}_{n}^{k}(\alpha,\boldsymbol{\lambda}) \\ &\text{s.t.} \quad \boldsymbol{C}_{me}^{k} \cdot \boldsymbol{Z}_{n}^{k} \le -\bar{g}_{me}^{k}, \\ &\quad \boldsymbol{Z}_{n,\min}^{k} \le \boldsymbol{Z}_{n}^{k} \le \boldsymbol{Z}_{n,\max}^{k} \end{aligned} \tag{10}$$

where $\boldsymbol{C}_{f,me}^{k}$ and $\boldsymbol{C}_{me}^{k}$ are the sensitivity vectors of e-th micro level set function associated with the objective function and volume constraint, $\boldsymbol{Z}_{n}^{k} = \alpha\left(\boldsymbol{C}_{f,me}^{k} + \lambda \boldsymbol{C}_{me}^{k}\right)$, $\bar{g}_{me}^{k}$ is the residual of e-the microscale volume constraint and the related shape sensitives are

$$\begin{cases} \boldsymbol{C}_{f,me}^{k}(\boldsymbol{y}^{B}) = -\left(\int_{\mathrm{D}_e} H(\phi_M)\varepsilon_{ij}^{k}\varepsilon_{kl}^{k}(\boldsymbol{x})d\mathrm{V}\right)\left(L\mathbb{E}_{pqrs}\left(\varepsilon_{rs}^{0} - \frac{\partial \chi_{e,r}^{ij}}{\partial y_s}\right)\left(\varepsilon_{pq}^{0} - \frac{\partial \chi_{e,p}^{kl}}{\partial y_q}\right)\right)(\boldsymbol{y}^{B}) \\ \boldsymbol{C}_{me}^{k}(\boldsymbol{y}^{B}) = L(\boldsymbol{y}^{B}) \end{cases}$$

(11)

with ε_{rs}^{0} denoting the unit strain tensors and $\boldsymbol{y}^{B}$ denoting associated boundary point.

With use of the optimal boundary movements, the macroscopic and microscopic structures can be obtained via (3). It should be noted that, on one hand, the optimal microstructures are affected by the macroscopic strain through (11); on the other hand, the macroscopic strain is determined by the macroscopic structure and the effective properties of microstructures. The optimal macrostructure and microstructures are inherently coupled [29]. With such coupling being ignored, the effective properties of the optimal microstructures may not be consistent in optimality with respect to the current macroscopic structure at intermediate iterations. However, as discussed in [29], it was observed that the inconsistency would vanish as a solution converges and has little effects on the final solution.

3.2 Connectivity of multiple microstructures

The L-beam example in Fig. 3(a) is considered to illustrate the multiscale optimization. The solid material is isotropic with Young's modulus $E = 1$ and Poisson's ratio $\nu = 0.3$. The structural domain is divided into 3 subregions with uniform microstructures distributed in each region. The upper bounds of volume fractions are $w_M = w_{me} = 40\%, e = 1, \ldots, 3$, respectively.

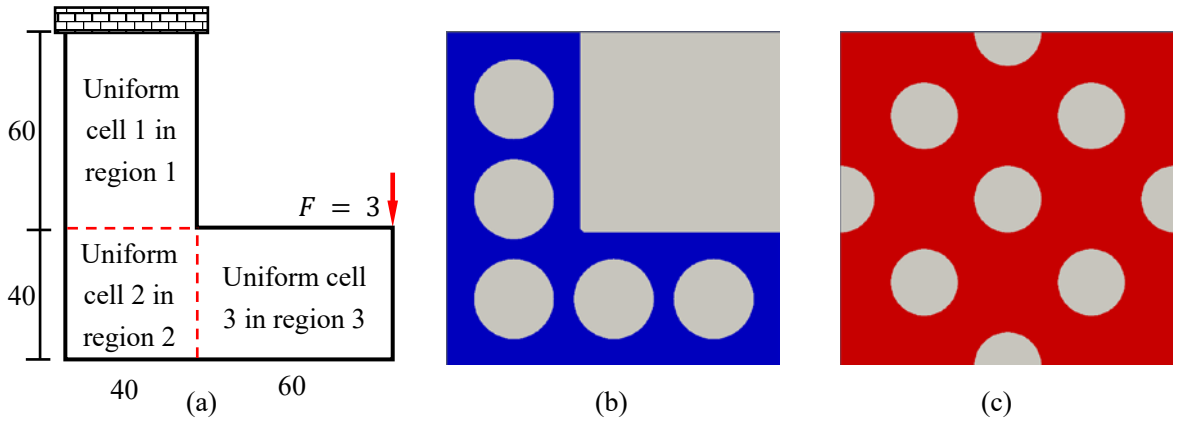

Fig. 3 An L-beam example with *(a)* the design domain, *(b)* the initial macroscale structure and *(c)* the initial microstructure

With the initial designs shown in Fig. 3 (b) and (c), we obtain the optimized multiscale structure shown in Fig. 4 with the optimal structural mean compliance 7295. The obtained macroscale structure is very similar as the single scale design result [30], which is reasonable. The three optimized microstructures, however, are not well-connected. In addition, they cannot transfer loads well in reality as expected by the homogenization theory. The multiscale structures are analyzed in the structural scale using the effective properties of microscopic unit cells and the scale separation assumption makes the structure unware of microstructural topologies. As a result, the effects of the connectivity between spatially varying microstructures cannot be considered in analysis hence, cannot be considered in design optimization.

In order to address this challenge in the multiscale design optimization framework, we introduce a quantity to measure the microstructural connectivity.

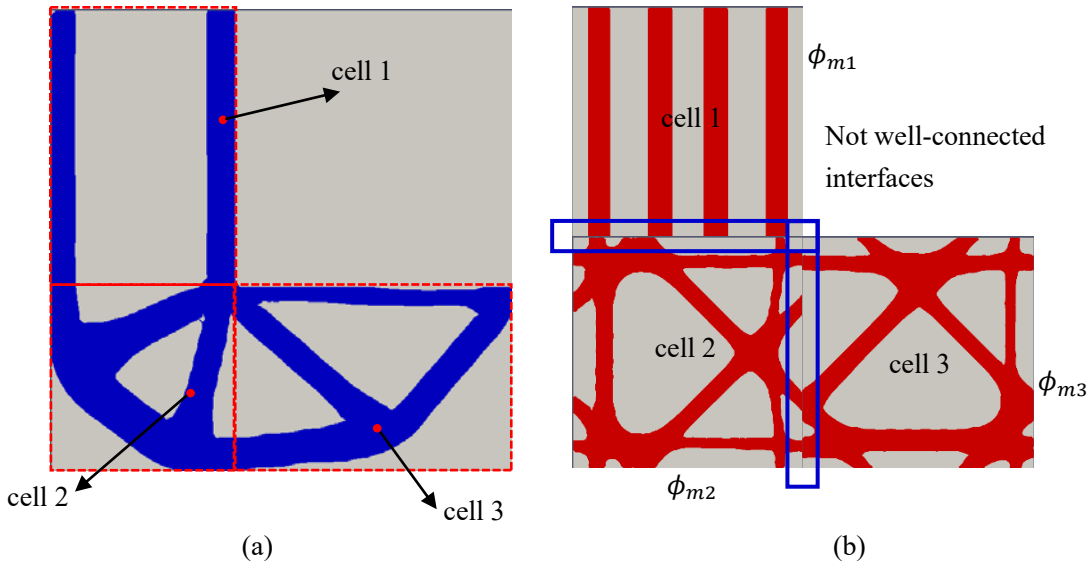

Fig. 4 Multiscale optimization solution of the L beam example *(a)* optimized macroscale structure and *(b)* optimized microstructures illustrating the connectivity challenges

4 Connectivity Index: Explicit Index to Quantify Connectivity between Two Unit Cells

Connectivity Index (CI) is defined using a local interface region of the mutual boundary, as shown Fig. 5. Considering the two strips from each unit cell, the following normalized parameter, CI can be defined:

$$CI \triangleq \frac{\sum_{i=1}^{2}\int_{\mathrm{Y}_i^{\mathrm{s}}} H\left(\phi_i(\boldsymbol{y})\right)\left(1-H\left(\phi_j(\mathbf{R}\boldsymbol{y})\right)\right)d\mathrm{Y}}{\sum_{i=1}^{2}\int_{\mathrm{Y}_i^{\mathrm{s}}} H\left(\phi_i(\boldsymbol{y})\right)d\mathrm{Y}}, \quad i\neq j; i,j=1,2 \qquad (12)$$

where $\mathrm{Y}_i^{\mathrm{s}}$ is the strip region colored in light red near the adjacent cell of i-th microstructure. $\mathbf{R}$ denotes the mirror reflection operator, which maps a point $\boldsymbol{y}$ to its symmetric counterpart $\mathbf{R}\boldsymbol{y}$ in the adjacent cell. CI is actually a symmetry measure of the material distribution in the interface region. Two unit cells are perfectly connected when $CI=0$, which implies that their connection regions are symmetric about the interface, while $CI=1$ is completely disconnected.

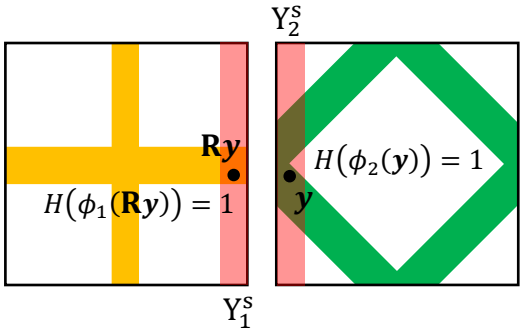

Fig. 5 An illustration of the proposed connectivity measure, where yellow structure on the left represents one-unit cell and the green structure on the right represents the adjacent unit cell, and the light red strips represent the interface regions used to quantify the connectivity between the two cells

In numerical implementation, CI can be calculated as

$$CI = 1 - \frac{\sum_{i=1}^{2}\int_{\mathrm{Y}_i^s} H\big(\phi_i(\boldsymbol{y})\big)H\left(\phi_j(\mathbf{R}\boldsymbol{y})\right)d\mathrm{Y}}{\sum_{i=1}^{2}\int_{\mathrm{Y}_i^s} H\big(\phi_i(\boldsymbol{y})\big)d\mathrm{Y}} \triangleq 1 - \frac{A_{\mathrm{sum2}}}{A_{\mathrm{sum1}}}, (i,j=1,2; i\neq j) \quad (13)$$

with $A_{\mathrm{sum1}} = \sum_{i=1}^{2}\int_{\mathrm{Y}_i^s} H\big(\phi_i(\boldsymbol{y})\big)d\mathrm{Y}$ and $A_{\mathrm{sum2}} = \sum_{i=1}^{2}\int_{\mathrm{Y}_i^s} H\big(\phi_i(\boldsymbol{y})\big)H\left(\phi_j(\mathbf{R}\boldsymbol{y})\right)d\mathrm{Y}$. Furthermore, the corresponding shape derivative with respect to the i-th microstructure can be written as:

$$CI'(\mathrm{Y}_i^s)\big(\boldsymbol{Z}_n^i\big) = \frac{A_{\mathrm{sum2}}\int_{\Gamma_i^s} Z_n^i d\mathrm{S} - 2A_{\mathrm{sum1}}\int_{\Gamma_i^s} H\big(\phi_i(\boldsymbol{y})\big)H\left(\phi_j(\mathbf{R}\boldsymbol{y})\right)Z_n^i d\Gamma}{A_{\mathrm{sum1}}^2} \quad (14)$$

where Γ_i^s denotes the microstructural boundary in the strip region Y_i^s.

For the proposed CI, one is required to select a suitable width of strip region. Generally, for a smaller width of the strip region, CI is more sensitive to the boundary movement; once the structural boundary moves out of the strip region Y_i^s, the sensitivity (14) would have no effect. A larger width would be numerically more stable and effective; however, it can potentially reduce the objective function to a greater extent. This will be discussed further in the numerical investigation.

We apply this with the level set topology optimization method for structural mechanics in this paper for illustration. However, we note that the proposed CI formulation is only a function of the material distribution and is independent of the physics of the problem. This means this constraint is applicable potentially to any topology optimization problems. Since we are introducing an additional constraint function into the problem formulation, this approach would be applicable with any topology optimization methods such as SIMP [30], ESO [31, 32] and MMC/MMV methods [33-36].

5 Connecting Microstructures in Homogenization-based Optimization

In this section, we investigate the use of CI in connecting two or more microstructures using homogenization-based topology optimization. Two formulations are investigated: (i) adding penalized CI to the objective function (ii) adding CI as a constraint. The following section first details the two formulations, followed by numerical examples.

5.1 Problem formulations

a) Penalization formulation

In this method, CI is added to the objective function of (10), i.e.,

$$f = f + \bar{M}(1 - \exp(-\bar{S}k))CI \tag{15}$$

where $\bar{M}$ is a weighting factor, $\bar{S}$ denotes the average of the sensitivity of f and k is the iteration number. In this way, the penalization term of CI is applied to the objective function gradually in order to not over-restrict the microstructures at the initial steps.

b) Constrained optimization formulation

The second formulation is to add CI as a constraint, i.e., $CI \leq \overline{CI}$ in (10) to enforce the microstructural connectivity. When determining the optimal boundary movements of the *e*-th microstructure, the CI-related constraint reads

$$\boldsymbol{C}^{k,me} \cdot \boldsymbol{Z}_n^k \leq -\overline{CI}^{k,me} \tag{16}$$

where $\overline{CI}^{k,me} = 1 - \frac{A_{\text{sum2}}^k}{A_{\text{sum1}}^k} - \overline{CI}$ and

$$\boldsymbol{C}^{k,me}(\boldsymbol{y}^B) = \begin{cases} \dfrac{A_{\text{sum2}}^k - 2A_{\text{sum1}}^k H\left(\phi^k(\mathbf{R}\boldsymbol{y}^B)\right)}{\left(A_{\text{sum1}}^k\right)^2}, & \text{if } \boldsymbol{y}^B \in \mathrm{Y}_i^s \quad (i,j = 1,2; i \neq j) \\ 0, & \text{otherwise} \end{cases} \tag{17}$$

5.2 Numerical example for single interface

The purpose of this section is to numerically investigate the connectivity index function within microstructure optimization and compare the two formulations of Section 5.1. We therefore, first construct particularly challenging two cell optimization problems with a single interface, where the optimized topologies of the two adjacent cells are completely disconnected. They are shown in Fig. 6. The first problem, Fig. 6(a) optimizes the left hand side cell for the maximum shear modulus and the right hand side cell for the maximum bulk modulus, i.e., $f_1(\mathbb{E}^{\mathrm{H}}) = -D_{33}^{\mathrm{H}}$ and $f_2(\mathbb{E}^{\mathrm{H}}) = -(D_{11}^{\mathrm{H}} + D_{22}^{\mathrm{H}} + D_{12}^{\mathrm{H}} + D_{21}^{\mathrm{H}})/4$. The second problem, Fig. 6(b), optimizes each cell for the maximum stiffness in the direction orthogonal to each other, i.e., $f_1(\mathbb{E}^{\mathrm{H}}) = -D_{11}^{\mathrm{H}}$ and $f_2(\mathbb{E}^{\mathrm{H}}) = -D_{22}^{\mathrm{H}}$ in the 3×3 effective elasticity constitutive matrix $\mathbf{D}^{\mathrm{H}}$.

These solutions are obtained by applying level set topology optimization with homogenization starting from a square domain with a circular hole in the center. For a general objective function related to the macroscopic effective property, $f(\mathbb{E}^{\mathrm{H}})$, the shape sensitivities for a boundary point $\boldsymbol{y}^B$ of a microstructure at the k-th iteration can be written as

$$C_f^k(\boldsymbol{y}^B) = -\frac{\partial f}{\partial E_{ijkl}^H}\left(L\mathbb{E}_{pqrs}\left(\varepsilon_{rs}^0 - \frac{\partial \chi_{e,r}^{ij}}{\partial y_s}\right)\left(\varepsilon_{pq}^0 - \frac{\partial \chi_{e,p}^{kl}}{\partial y_q}\right)\right)(\boldsymbol{y}^B) \qquad (18)$$

Following the procedure outlined in Section 2, optimal microstructures can be obtained.

Due to the periodic boundary condition, each cell optimization is unaware of its adjacent cell and the resulting topologies are completely disconnected (the interface regions are highlighted with dotted lines). In practice, these solutions cannot transfer loads between two adjacent cells and are only fictitious designs. For all solutions, $E = 1$ and $\nu = 0.3$ with $w_1 = w_2 = 40\%$ were used.

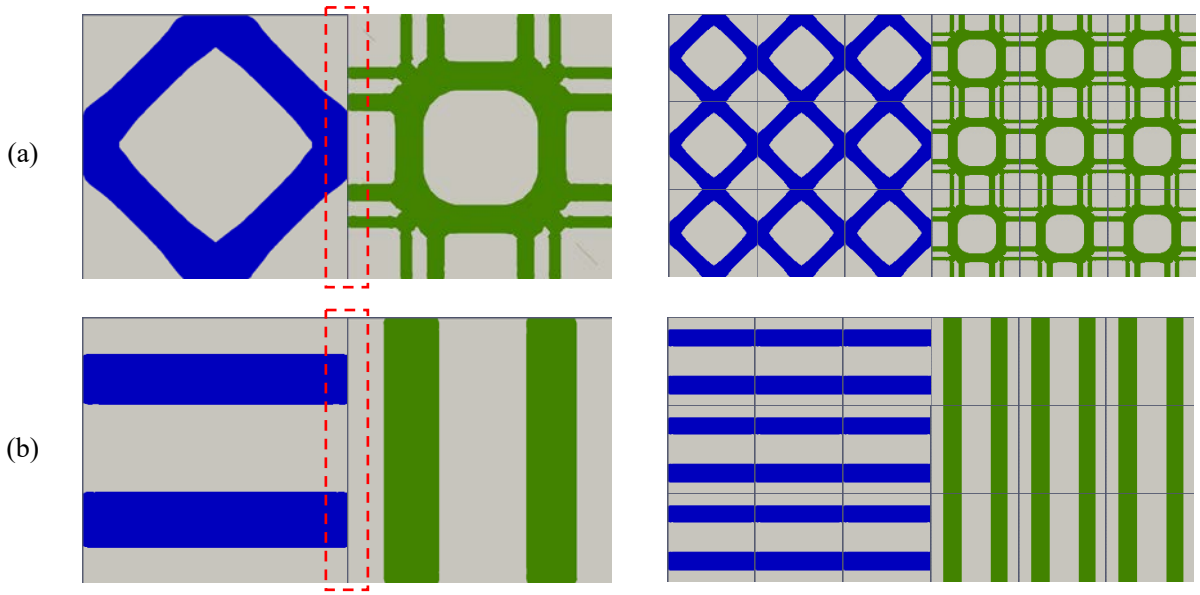

Fig. 6 Two test cases obtained by microstructural optimization via homogenization, *(a)* maximum shear modulus and bulk modulus solutions and *(b)* maximum D_{11}^{H} and D_{22}^{H} solutions

5.2.1 Application of the penalization approach

Tables 1 and 2 summarize the optimized solutions obtained by adding CI as a penalized objective with a range of weighting factors, $\bar{M}$. The design domains were discretized by 50×50 bilinear elements and the widths of strip regions $\mathrm{Y}_i^{\mathrm{s}}$ are set as 1 element-width. It is observed that as the weighting factor increased, the resulting topological solutions connected at the interface. It is anticipated that the effects of CI would reduce the moduli of the optimal solutions. As seen in Table 1, the reduction of the optimal objective function relative to those of the optimized solutions without CI is less than 2%. However, for inappropriate weight factors, step changing similar as Fig. 1(b) still exists. This is due to the fact that the penalization approach comes from the multi-objective optimization, and selecting appropriate weighting factor for converting it to a single-objective optimization is a trivial task and would be very difficult when multiple interfaces are involved.

Table 1 Optimized solutions for the maximum shear and bulk moduli cases by the penalization approach

$\bar{M}$	CI	Optimal solutions	Shear modulus	Bulk modulus	Decrease in modulus relative to $\bar{M}=0$	
0	1.00	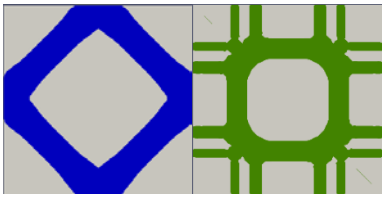	0.109	0.137	-	-
0.03	0.69	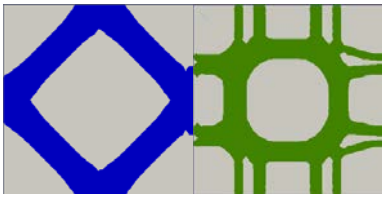	0.109	0.137	0.0%	0.0%
0.43	0.08	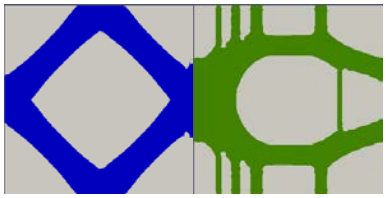	0.109	0.136	0.0%	0.73%
2.5	0.04	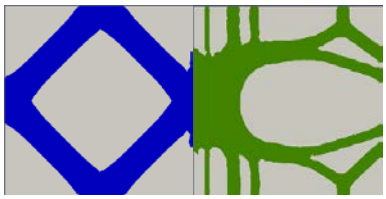	0.106	0.135	2.75%	1.46%

Table 2 Optimized solutions for the maximum D_{11}^{H} and D_{22}^{H} cases by the penalization approach

$\bar{M}$	CI	Optimal solutions	D_{11}^{H}	D_{22}^{H}	Decrease in modulus relative to $\bar{M}=0$	
0	1.00	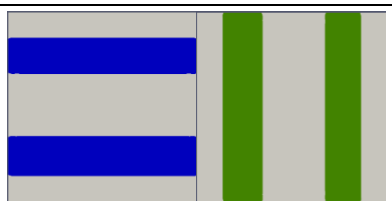	0.400	0.400	-	-

0.10	1.00	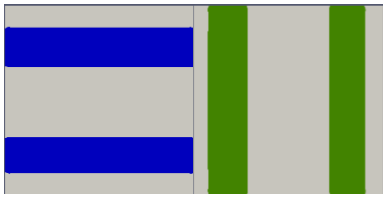	0.400	0.400	0.0%	0.0%
0.97	0.19		0.400	0.399	0.0%	0.25%
4.6	0.00		0.356	0.398	11.0%	0.25%

5.2.2 Application of the constraint approach

Tables 3 and 4 summarize the optimized solutions obtained by adding CI as a constraint with different upper bounds on CI and the widths of strip region (number of elements n_w in strip region). The optimized topologies show improved connectivities. It is observed that: (1) by adding different upper bounds of CI, the connectivity can be controlled quantitatively and explicitly during inverse homogenization; (2) as the CI constraint reduces, the connectivity improves and this is at the expense of the objective function values; (3) the maximum relative reduction of the optimal objective function values is no more than 3% as compared to their disconnected counterpart. Experiences with a range of numerical investigations indicate that a reasonably good connectivity is usually achieved with $\overline{CI} = 0.10$, which may need to be smaller for a wider interface region.

Table 3 Optimized solutions for the maximum shear and bulk moduli cases by the constraint approach

n_w	$\overline{CI}$	Optimal designs	Shear modulus	Bulk modulus	Decrease in modulus

							relative to $n_w = 0$
(a)	1	0.83	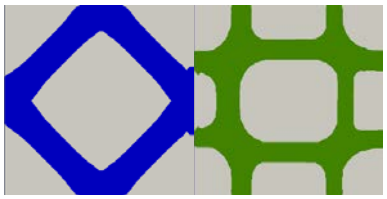	0.109	0.136	0.0%	0.73%
(b)	1	0.50	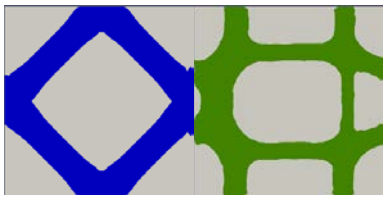	0.109	0.135	0.0%	1.46%
(c)	1	0.25	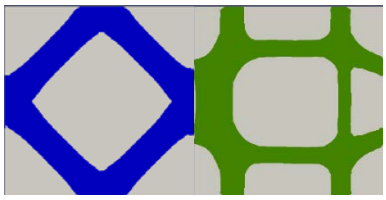	0.109	0.135	0.0%	1.46%
(d)	1	0.05	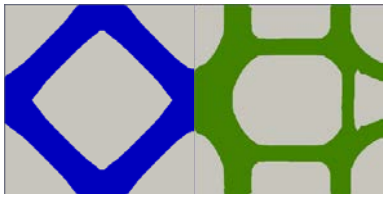	0.109	0.134	0.0%	2.19%
(e)	2	0.10	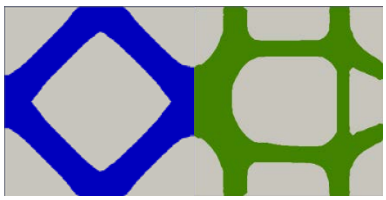	0.109	0.133	0.0%	2.92%
(f)	6	0.10	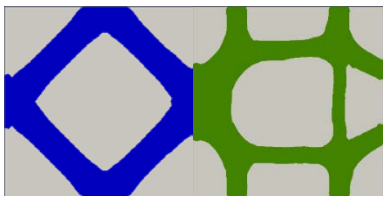	0.109	0.133	0.0%	2.92%

Table 4 Optimized solutions for the maximum D_{11}^{H} and D_{22}^{H} cases by the constraint approach

n_w	$\overline{CI}$	Optimal designs	D_{11}^{H}	D_{22}^{H}	Decrease in modulus relative to $n_w = 0$

(a)	1	0.70		0.400	0.400	0.0%	0.0%
(b)	1	0.35		0.398	0.400	0.5%	0.0%
(c)	1	0.10		0.400	0.398	0%	0.5%

5.3 Numerical example for multiple interfaces

5.3.1 Multiple interfaces

We now apply the CI constraint to multiple interfaces. Three microstructural optimized solutions with a 40% volume constraint are used in this study: (1) maximum shear modulus, (2) maximum bulk modulus and (3) maximum D_{22}^{H}. For these results, we use the initial design with five circular holes, Fig. 7(a). As a result, the resulting optimal topologies of Fig. 7(b)-(d) are slightly different from those using the one-hole initial solution (Fig. 6) reflecting the non-convex nature of microstructural optimization [7, 29]; however, the objective functions of these solutions are different only by around 1% (0.110 (maximum shear modulus), 0.138 (maximum bulk modulus) and 0.400 (maximum D_{22}^{H}) for the five-hole initial solution in comparison with 0.109, 0.136 and 0.400 for the one-hole initial solution). These provide additional optimized topologies to challenge the CI function.

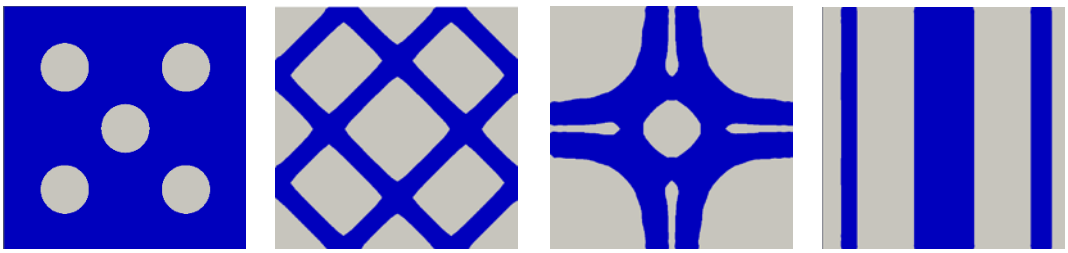

(a) (b) (c) (d)

Fig. 7 *(a)* Initial design with five circular holes, *(b)* optimal unit cell with maximum shear modulus, *(c)* optimal unit cell with maximum bulk modulus and *(d)* optimal unit cell with maximum D_{22}^{H}

Table 5 presents 1×3 and 2×2 microstructures optimized for the maximum shear modulus, maximum bulk modulus and maximum D_{22}^{H} from different initial designs. In the 1×3 microstructures examples, the unit cells in the left and right side are added by one CI constraint, the middle unit cells are constrained by two CIs. Two CI constraints are added to each cell in the 2×2 case during the inverse homogenization. With $\overline{CI} = 0.10$ and $n_w = 1$, Table 5 demonstrates that the connectivities are improved substantially. For all cases, the maximum moduli were reduced by no more than 3%.

Table 5 Optimized microstructures with and without connectivity constraints

Without considering connectivity	With connectivity constraints
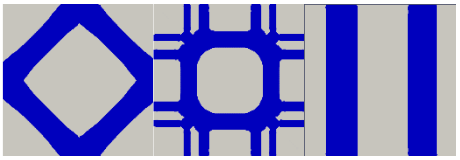	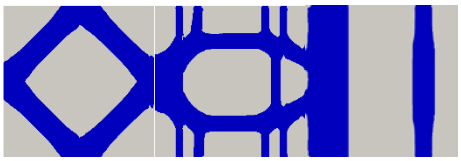
	

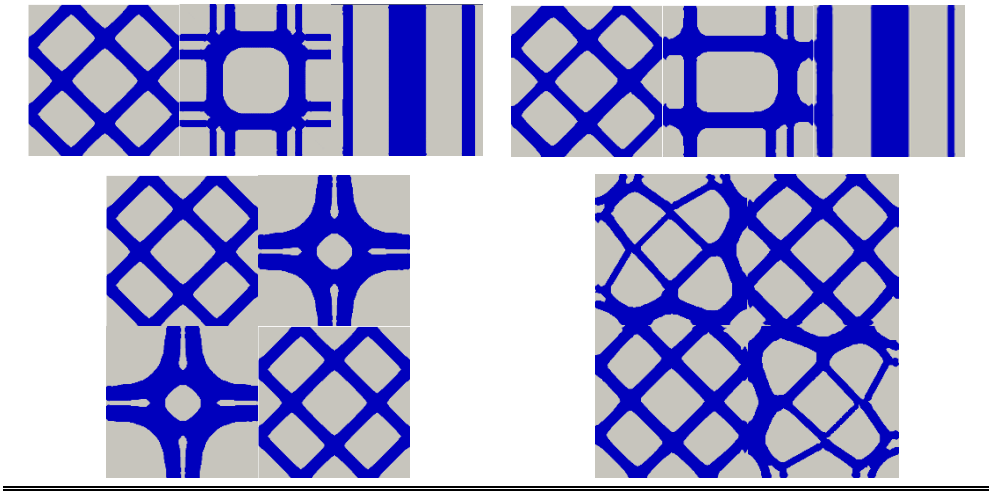

5.3.2 Self-connectivity

The efforts above focused on improving the connectivity between two adjacent microstructures. By applying the connectivity constraint, the connection between different cells will be greatly improved while the symmetry of unit cells can be broken. Subsequently, the connectivity (i.e., symmetry of the interface region) between the same unit cells (e.g., the connection of the right-side unit cells in Fig. 8) may not as perfect as the connectivity of different unit cells.

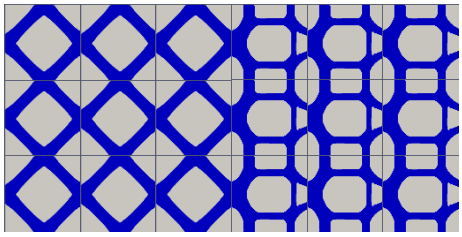

Fig. 8 The maximum shear and bulk microstructure design

If one wants to further improve the self-connectivity of the microstructures, the CI constraint can also be applied to each cell as shown in Fig. 9(a), i.e.,

$$CI_{\text{self}} = 1 - \frac{\int_{\text{Y}^{\text{S}} \cup \mathbf{R}'\text{Y}^{\text{S}}} H\big(\phi(\boldsymbol{y})\big) H\big(\phi(\mathbf{R}'\boldsymbol{y})\big) d\text{Y}}{\int_{\text{Y}^{\text{S}} \cup \mathbf{R}'\text{Y}^{\text{S}}} H\big(\phi(\boldsymbol{y})\big) d\text{Y}} \leq \overline{CI}_{\text{self}} \tag{19}$$

with $\mathbf{R}'\boldsymbol{y}$ denoting the symmetric point of $\boldsymbol{y}$ in the same unit cell and $\mathbf{R}'\mathrm{Y}^{\mathrm{S}}$ is the symmetric strip region of Y^{S}. By adding the CI constraint to the maximum shear and bulk microstructure design problem with $\overline{CI}_{\mathrm{self}} = 0.10$ and $n_w = 1$, the self-connectivity property of cells can be improved, contrast Fig. 9(b) with Fig. 8.

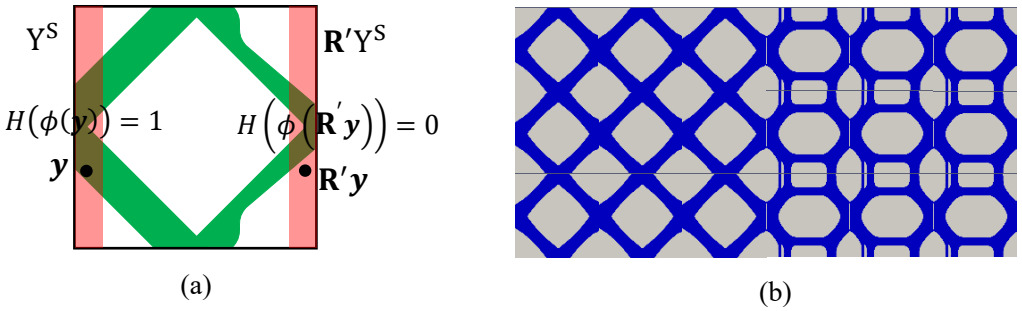

Fig. 9 *(a)* Illustration of the self-connectivity index and *(b)* maximum shear and bulk modulus microstructure designs with self-connectivity constraints

It should be noted that, due to numerical errors and limitation of optimizer, the obtained designs can hardly achieve a perfect connection (i.e. $CI = 0$). However, it is expected that, only a 'minor' postprocessing is required to smooth the part in the interface region to finally improve the connectivity, and such treatment would have very small influence on the optimality of the microstructures.

6 Multiscale Topology Optimization with Connectivity

We return to multiscale optimization in Section 3 and apply additional CI constraints to enforce connectivity between the microstructural regions. This is achieved by adding the CI constraints only at the microstructural scale in the decomposed optimization problem. For the e-th microstructure with a number of T boundaries interfacing different microstructures, (20) is added to obtain the optimal boundary movement at k-th step:

$$\boldsymbol{C}_l^{k,me} \cdot \boldsymbol{Z}_n^{k,me} \leq -\overline{CI}_l^{k,me}, l = 1,..,T \tag{20}$$

It is noted that the CI constraint of the e-th microstructure is dependent on its adjacent cells, in other words, the connectivity constraint couples the adjacent microstructures together. In the current investigation, such a coupling is ignored for simplicity and CI is updated iteratively, i.e., $\overline{CI}_l^{k,me} = 1 - \frac{A_{\text{sum2}}^k}{A_{\text{sum1}}^k}\left(\phi_e^k, \phi_{n_l}^k\right) - \overline{CI}_l^{me}$ with $\overline{CI}_l^{me}$ denoting the CI upper bound for the connectivity between e-th and n_l-th unit cells. The following numerical results indicate that this approximation is reasonable.

6.1 Cantilevered beam

The first example considers two cantilevered beams shown in Fig. 10. The beams are divided into two regions each of which can take different microstructures and the microstructure within a region is uniform. Here only the microstructures are optimized for the minimum compliance computed at the macroscopic scale and the macroscopic topology is fixed to be solid. The upper bound for the microscopic volume fraction is set at 40% and the CI constraint at 0.10. The Young's modulus is set to be 1 and Poisson's ratio 0.3. The unit cell is discretized by 100×100 bilinear plane stress elements and the initial design contained a hole of radius 25 at the center.

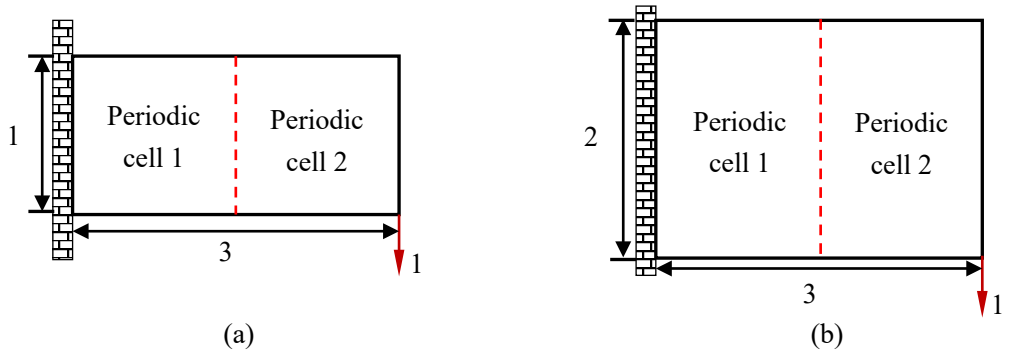

Fig. 10 Cantilevered beam *(a)* design domain 1:3 and *(b)* design domain 2:3

The optimized solutions are summarized in Tables 6 and 7 for a range of the strip width, n_w. As can be observed, all microstructures are connected and in that sense they are manufacturable and realistic. However, the discrete member size changes in lower n_w would lead to poor load transfer between different type of cells and reduce the mechanical performance of optimal designs. The member size changes become more continuous as n_w increases. As would be expected, this has an effect of increasing the objective function however, the increases are observed to be small (less than 2%). Figure 11 illustrates an example of the repeated cellular materials in the cantilevered beams.

Table 6 Optimized solutions for cantilevered beam 1:3

n_w	Optimal microstructures	CI	Mean compliance	Increase in compliance relative to $n_w = 0$
0	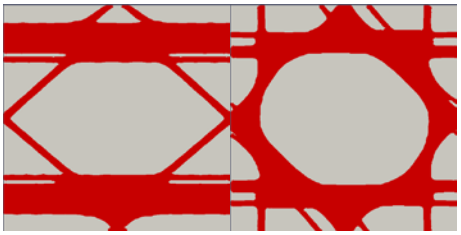	0.44	474	-
1	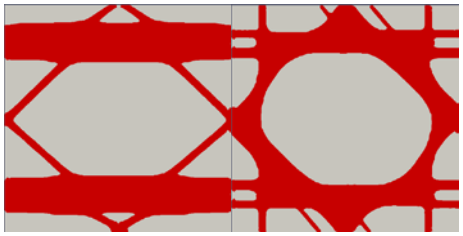	0.21	476	0.42%
5		0.10	477	0.63%

Table 7 Optimized solutions for cantilevered beam 2:3

n_w	Optimal microstructures	CI	Mean compliance	Increase in compliance relative to $n_w = 0$
0		0.42	130	-
1	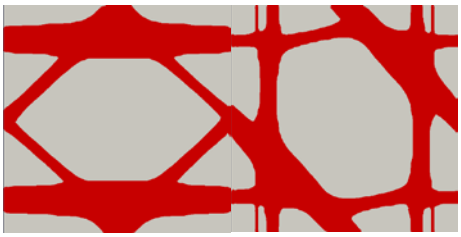	0.23	131	0.77%
5		0.10	132	1.54%

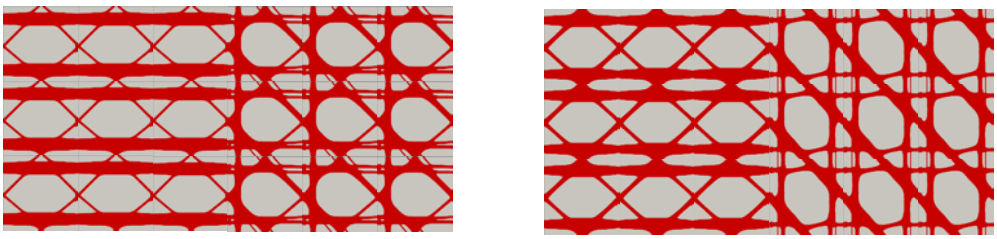

(a) (b)

Fig. 11 Illustrations of the connected cellular materials of the cantilevered beams *(a)* design domain 1:3 and (b) design domain 2:3

We note that the constraints are not satisfied in some solutions shown in Tables 6 and 7. In order to investigate this, we examine the optimization history of the cantilevered beam of 2:3, Fig. 12 which is representative of both of the cantilevered beams. It can be seen that the structural mean compliances converge smoothly for all cases and the strip width n_w does not have a significant influence. The n_w constraint

oscillates particularly when n_w is small, e.g., $n_w = 1$. This is because when n_w is small, even a small perturbation of the boundary can have a significant influence on the CI value. Increasing the strip width, e.g., $n_w = 5$, has an effect of relaxing the constraint and the oscillation reduces leading to a more stable convergence and meeting the specified constraint. It can be deduced from this that an adaptive CI constraint may lead to a stable convergence and this will be investigated further in the following section.

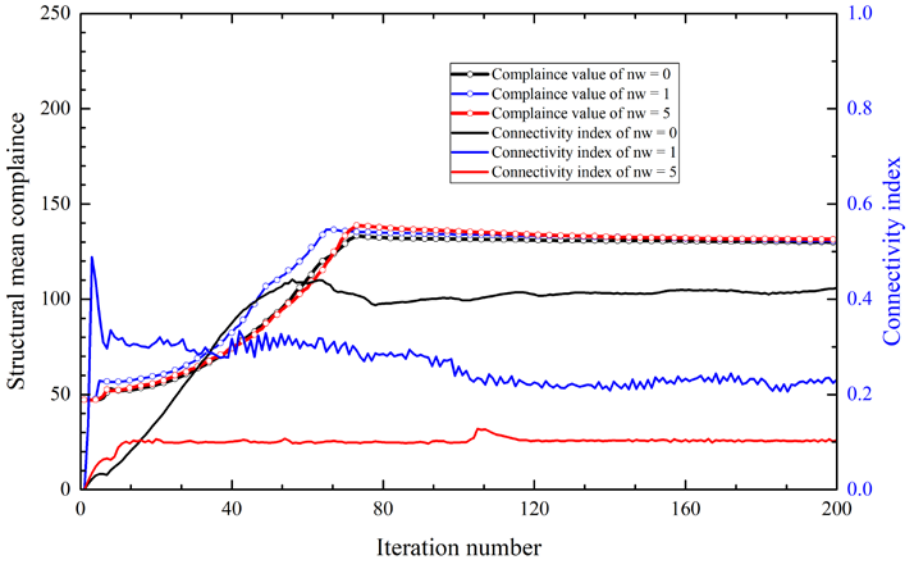

Fig. 12 Optimization history of cantilevered beam 2:3

6.2 L-beam

We now consider the L-beam shown in Section 3 to minimize the overall structural compliance with three regions are specified to have different material architectures. In this case, the topologies are optimized both at the macroscopic and the microscopic scales. Since there are three material microstructures, two CI constraints are added to the microscale optimization (to get a better connection as well as preserving the original optimality, the CI bounds are set as 0.08 for this example). Three cases are considered using the following parameters with the last case adopting the adaptive CI constraints:

1. $n_w = 2,\ \overline{CI}_1 = \overline{CI}_2 = 0.08;$

2. $n_w = 10,\ \overline{CI}_1 = \overline{CI}_2 = 0.08$;
3. $n_w = 10,\ \overline{CI}_1 = \overline{CI}_2 = \max\{0.08, 1 - 0.01k\}$.

The multiscale optimized solutions are shown in Figs. 13-15 with the objective function and CI values in Table 8. Fig. 13 with a small strip region, $n_w = 2$, shows that the microstructures at interface 1 is not well connected ($CI_1 = 0.24$ and $CI_2 = 0.10$). As seen in the previous example in Section 6.1, for Case 2, increasing the strip width to $n_w = 10$ leads to a solution that satisfy both of the CI constraints, i.e. $CI_1 = 0.08$ and $CI_2 = 0.07$, with relative increase of objective function value by 2.97%. However, an additional horizontal bar (marked by dash-dotted circle) is generated to satisfy the CI constraint. Furthermore, the iteration history of Case 2 illustrated in Fig. 15 reveals that the optimizer tried to satisfy the CI constraints every step and this may be overly restricting the search space for the microstructure.

The adaptive constraint in Case 3 is introduced to avoid such issues as the CI constraints are not strictly enforced from the beginning. This offers a greater level of design freedom for the microstructures during the early stages of optimization. Fig. 16 shows the microstructural solutions that are well-connected at the interfaces with $CI_1 = 0.08$ and $CI_1 = 0.04$. Moreover, the overall compliance increase is only 0.77%. Fig. 17 shows the optimization history of the L-beam Case 3 with the adaptive CI constraints. The CI constraints are inactive at the beginning and the CI values grow quickly. After about 30 iterations, both of the CI values start to decrease and stabilize around 120 iterations. It should be point out that, due to the connectivity constraint which requires the material distribute symmetrically in the interface region, the material distribution in the interface region (e.g., variable thickness of unit cell 1) is not optimal from a point of view on pure-stiffness. This will be considered in the future work.

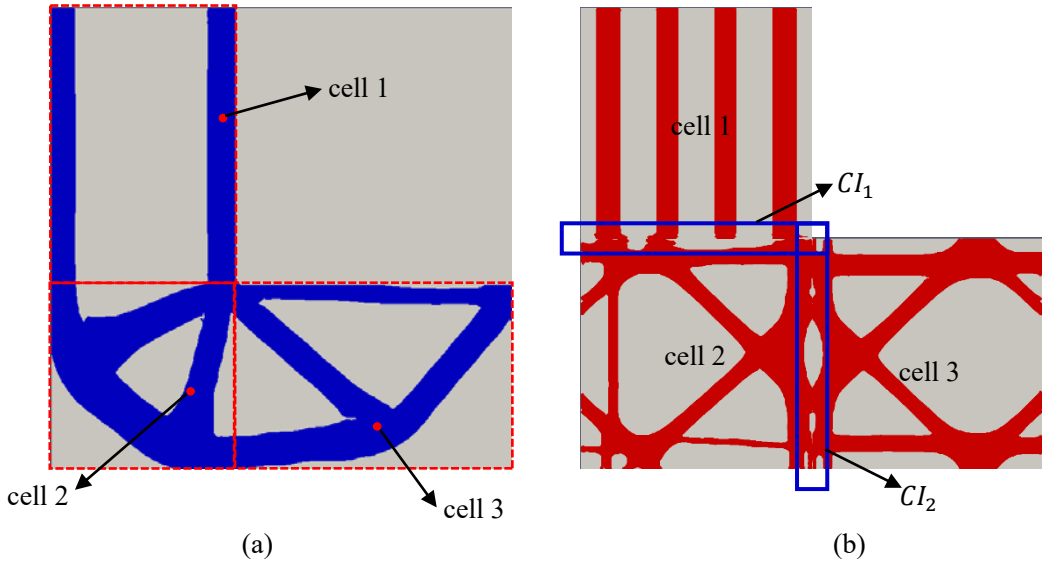

Fig. 13 Optimized solution for Case 1 *(a)* macrostructure and *(b)* microstructure

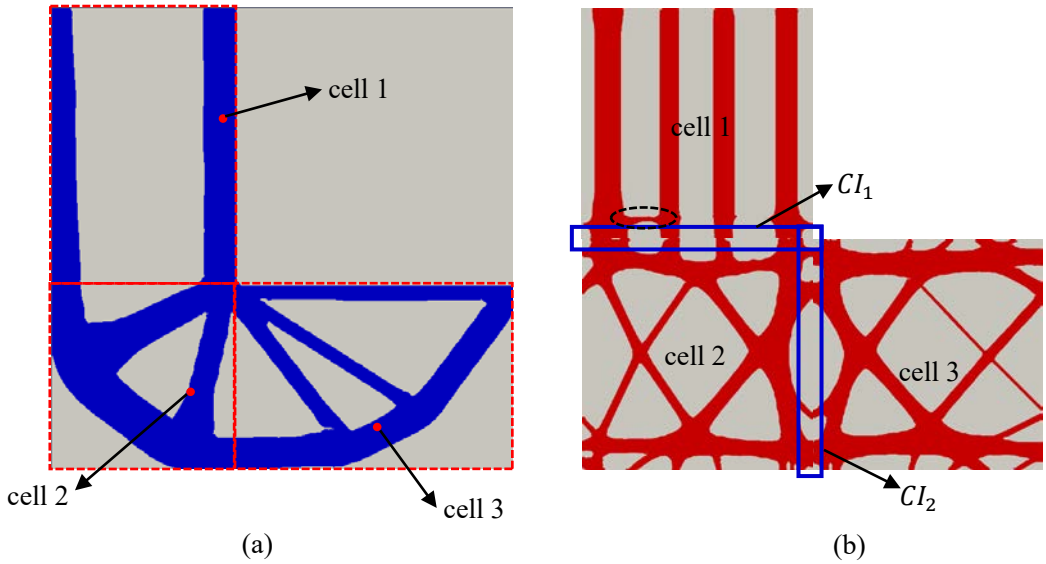

Fig. 14 The optimized multiscale structure of case (3) with *(a)* the optimal macrostructure and *(b)* the optimal microstructures

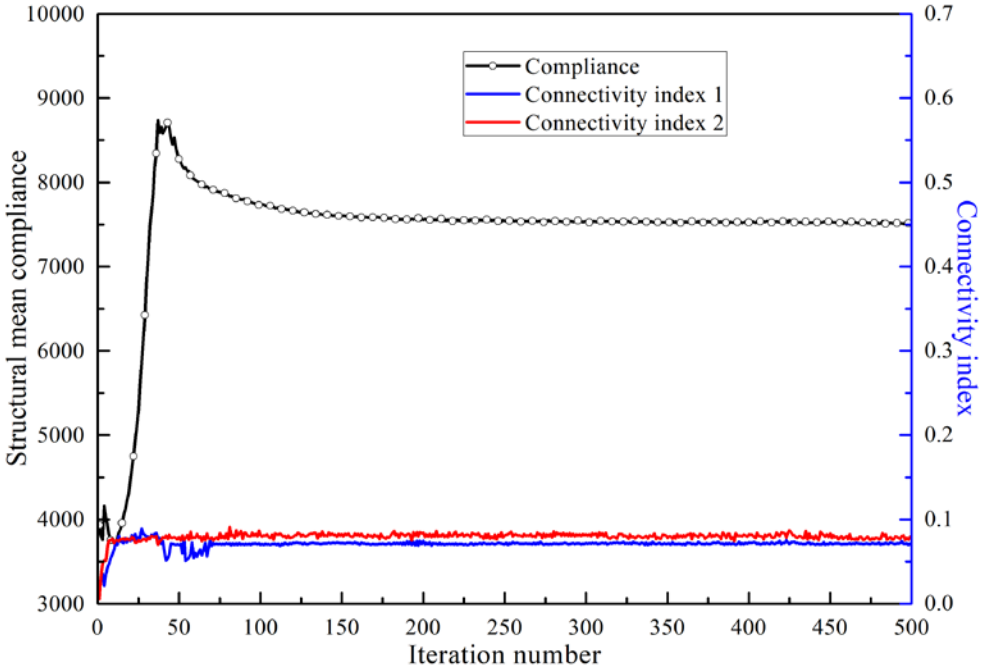

Fig. 15 Optimization history of L-beam Case 2

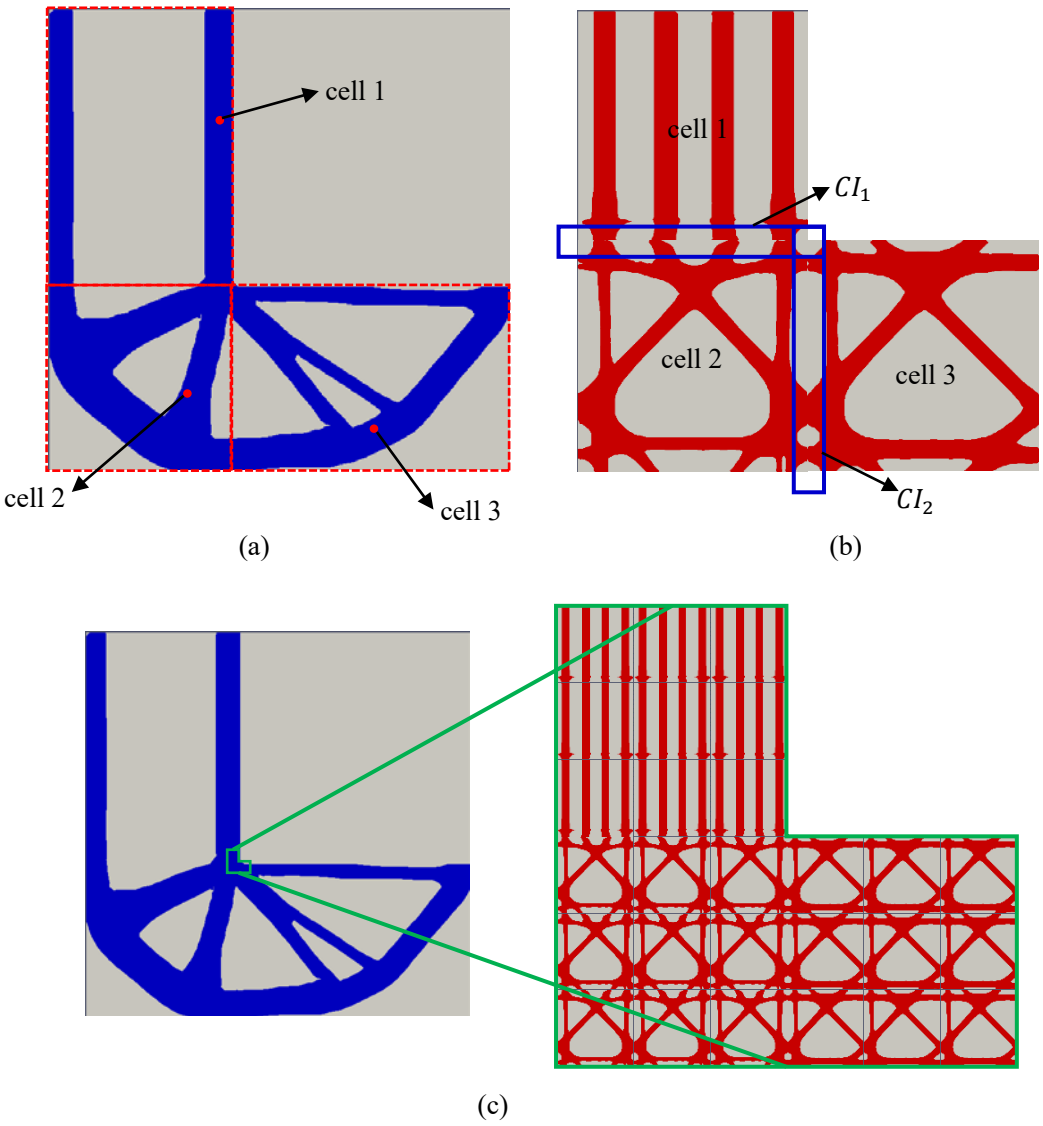

Fig. 16 Optimized solution for Case 3 *(a)* macrostructure and *(b)* microstructure and *(c)* an illustration of the optimized structure-material system

Table 8 Objective and constraint function values for L-beam solutions

n_w	$\overline{CI}_1 = \overline{CI}_2$	Compliance	Increase in compliance relative to n_w=0	CI_1	CI_2
0	-	7295	-	0.47	0.41
2	0.08	7338	0.59%	0.24	0.10

10	0.08	7518	2.97%	0.08	0.07
10	$\max\{0.08, 1-0.01k\}$	7351	0.77%	0.08	0.04

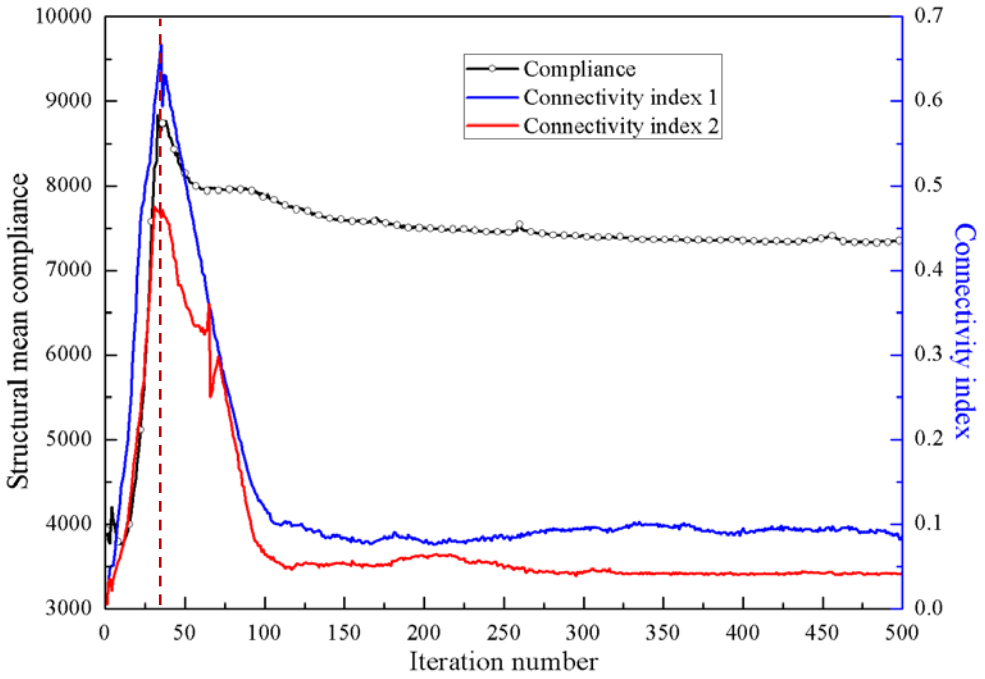

Fig. 17 Optimization history of L-beam Case 3

7 Concluding remarks

Connectivity Index (CI) is formulated as a quantified measure of the connectivity between two adjacent microstructures. The CI function was introduced to the optimization problem, firstly into the objective function and secondly as an explicit constraint. The numerical investigations were conducted to explore the effects of the two different formulations as well as the interface region widths for a range of problems in which the microstructures are optimized via the homogenization approach. The introduction of the CI functions was demonstrated to improve the connectivity at the interfaces substantially. As an additional constraint can reduce the design space and restrict the search, the objective function values of the final solutions are expected to be compromised. The numerical investigations show, however, that the increase is minimal, mostly in the order of 1%. It was observed there were cases that a solution

that satisfied the strict CI constraint could not be found or the optimizer found a trivial solution where the connectivity is achieved by making the interface region solid. In such cases, an adaptive strategy where the CI constraint was relaxed in the early stages of optimization and this gave the optimizer the freedom required to find good microstructure topologies. As optimization progresses and the number of iteration increases, the CI constraint is enforced more strictly yielding a satisfactory solution with the minimal increase in the objective function. It is noted that the CI function is completely geometry dependent and independent of the physics of the environment, therefore, the CI function approach is applicable to multiphysics topology optimization and this will be explored in our follow up study.

Acknowledgements

The authors acknowledge the support from DARPA (Award number HR0011-16-2-0032). H Alicia Kim also acknowledges the support of the Engineering and Physical Sciences Research Council Fellowship for Growth (grant number EP/M002322/2).

References

[1] Corni, I., Harvey, T. J., Wharton, J. A., Stokes, K. R., Walsh, F. C., and Wood, R. J. K., 2012, "A review of experimental techniques to produce a nacre-like structure," Bioinspir. Biomim., 7(3), p. 031001.

[2] Tan, T., Rahbar, N., Allameh, S. M., Kwofie, S., Dissmore, D., Ghavami, K., and Soboyejo, W. O., 2011, "Mechanical properties of functionally graded hierarchical bamboo structures," Acta Biomater., 7(10), pp. 3796-3803.

[3] Wickham, S., Large, M. C., Poladian, L., and Jermiin, L. S., 2006, "Exaggeration and suppression of iridescence: the evolution of two-dimensional butterfly structural colours," J. R. Soc. Interface, 3(6), pp. 99-109.

[4] Shalaev, V. M., 2007, “Optical negative-index metamaterials,” Nat. Photonics, 1(1), pp. 41-48.

[5] Zheng, X., Lee, H., Weisgraber, T. H., Shusteff, M., DeOtte, J., Duoss, E. B., Kuntz, J. D., Biener, M. M., Ge, Q., and Jackson, J. A., 2014, “Ultralight, ultrastiff mechanical metamaterials,” Science, 344(6190), pp. 1373-1377.

[6] Andreassen, E., Lazarov, B. S., and Sigmund, O., 2014, “Design of manufacturable 3D extremal elastic microstructure,” Mech. Mater., 69(1), pp. 1-10.

[7] Takezawa, A., Kobashi, M. and Kitamura, M., 2015. “Porous composite with negative thermal expansion obtained by photopolymer additive manufacturing,” APL Mater., 3(7), p. 076103.

[8] Berger, J. B., Wadley, H. N. G., and McMeeking, R. M., 2017, “Mechanical metamaterials at the theoretical limit of isotropic elastic stiffness,” Nature, 543, pp. 533-537.

[9] Sigmund, O., 1994, “Materials with prescribed constitutive parameters: an inverse homogenization problem,” Int. J. Solids Struct., 31(17), pp. 2313-2329.

[10] Sigmund, O., and Torquato, S., 1997, “Design of materials with extreme thermal expansion using a three-phase topology optimization method,” J. Mech. Phys. Solids, 45(6), pp. 1037-1067.

[11] Rodrigues, H., Guedes, J. M., and Bendsøe, M. P., 2002, “Hierarchical optimization of material and structure,” Struct. Multidiscip. Optim., 24(1), pp. 1-10.

[12] Coelho, P. G., Fernandes, P. R., Guedes, J. M., and Rodrigues, H. C., 2008, “A hierarchical model for concurrent material and topology optimisation of three-dimensional structures,” Struct. Multidiscip. Optim., 35(2), pp. 107-115.

[13] Liu, L., Yan, J., and Cheng, G., 2008, “Optimum structure with homogeneous optimum truss-like material,” Comput. Struct., 86(13), pp. 1417-1425.

[14] Niu, B., Yan, J., and Cheng, G., 2009, “Optimum structure with homogeneous optimum cellular material for maximum fundamental frequency,” Struct. Multidiscip. Optim., 39(2), pp. 115-132.

[15] Yan, J., Guo, X., and Cheng, G., 2016, “Multi-scale concurrent material and structural design under mechanical and thermal loads,” Comput. Mech., 57(3), pp. 437-446.

[16] Sivapuram, R., Dunning, P. D., and Kim, H. A., 2016, “Simultaneous material and structural optimization by multiscale topology optimization,” Struct. Multidiscip. Optim., 54(5), pp. 1267-1281.

[17] Guedes, J., and Kikuchi, N., 1990, “Preprocessing and postprocessing for materials based on the homogenization method with adaptive finite element methods,” Comput. Methods Appl. Mech. Eng., 83(2), pp. 143-198.

[18] Alexandersen, J., and Lazarov, B. S., 2015, “Topology optimisation of manufacturable microstructural details without length scale separation using a spectral coarse basis preconditioner,” Comput. Methods Appl. Mech. Eng., 290, pp. 156-182.

[19] Xie, Y. M., Zuo, Z. H., Huang, X., and Rong, J. H., 2012, “Convergence of topological patterns of optimal periodic structures under multiple scales,” Struct. Multidiscip. Optim., 46(1), pp. 41-50.

[20] Coelho, P. G., Amiano, L. D., Guedes, J. M., and Rodrigues, H. C., 2016, “Scale-size effects analysis of optimal periodic material microstructures designed by the inverse homogenization method,” Comput. Struct., 174, pp. 21-32.

[21] Dumontet, H., 1985. “Boundary layers stresses in elastic composites,” In Studies in Applied Mechanics (Vol. 12, pp. 215-232). Elsevier.

[22] Liu, C., Zhang, W., Du, Z., and Guo, X., “Multidomain topology optimization of manufacturable microstructures using homogenization method,” submitted.

[23] Zhou, S., and Li, Q., 2008, “Design of graded two-phase microstructures for tailored elasticity gradients,” J. Mater. Sci., 43(15), pp. 5157-5167.

[24] Radman, A., Huang, X., and Xie, Y. M., 2013, “Topology optimization of functionally graded cellular materials”, J. Mater. Sci., 48(4), pp. 1503-1510.

[25] Deng, J., and Chen, W., 2017, “Concurrent topology optimization of multiscale structures with multiple porous materials under random field loading uncertainty,” Struct. Multidiscip. Optim., 56(1), pp. 1-19.

[26] Wang, Y., Chen, F., and Wang, M. Y., 2017, “Concurrent design with connectable graded microstructures,” Comput. Methods Appl. Mech. Eng., 317, pp. 84-101.

[27] Dunning, P. D., and Kim, H. A., 2015, “Introducing the sequential linear programming level-set method for topology optimization,” Struct. Multidiscip. Optim., 51(3), pp. 631-643.

[28] Johnson, S. G., 2014, “The NLopt nonlinear-optimization package.”

[29] Xia, L., and Breitkopf, P., 2014, “Concurrent topology optimization design of material and structure within nonlinear multiscale analysis framework,” Comput. Methods Appl. Mech. Eng., 278, pp. 524-542.

[30] Bendsøe, M. P., and Sigmund, O., 2004, *Topology Optimization: Theory, Methods and Applications*, Springer, Berlin.

[31] Xie, Y. M., and Steven, G. P., 1993, “A simple evolutionary procedure for structural optimization,” Comput. Struct., 49, pp. 885-896.

[32] Querin, O. M., Steven, G. P., and Xie, Y. M., 1998, “Evolutionary structural optimisation (ESO) using a bidirectional algorithm,” Eng. Comput., 15, pp. 1031-1048.

[33] Guo, X., Zhang, W., and Zhong, W., 2014, “Doing topology optimization explicitly and geometrically - a new moving morphable components based framework,” ASME J. Appl. Mech., 81, p. 081009.

[34] Guo, X., Zhang, W., Zhang, J., and Yuan, J., 2016, “Explicit structural topology optimization based on moving morphable components (MMC) with curved skeletons,” Comput. Methods Appl. Mech. Eng., 310, pp. 711-748.

[35] Zhang, W., Yuan, J., Zhang, J., and Guo, X., 2016, “A new topology optimization approach based on Moving Morphable Components (MMC) and the ersatz material model,” Struct. Multidiscip. Optim., 53(6), pp. 1243-1260.

[36] Zhang, W., Yang, W., Zhou, J., Li, D., and Guo, X., 2017, “Structural topology optimization through explicit boundary evolution,” ASME J. Appl. Mech., 84, p. 011011.